FRONTIERS OF PHYSICS

RESEARCH ARTICLE
Volume 19 / Issue 4 / 43202 / 2024

Room-temperature ferroelectricity in van der Waals SnP_2S_6

Chaowei He[1,*], Jiantian Zhang[1,*], Li Gong[2], Peng Yu[1,†]

1 State Key Laboratory of Optoelectronic Materials and Technologies Guangzhou Key Laboratory of Flexible Electronic Materials and Wearable Devices Nanotechnology Research Center, School of Materials Science and Engineering, Sun Yat-sen University, Guangzhou 510275, China
2 Instrumental Analysis and Research Center, Sun Yat-sen University, Guangzhou 510275, China
*These two authors contributed equally to this work.
Corresponding author. E-mail: †yupeng9@mail.sysu.edu.cn
Received September 27, 2023; accepted November 13, 2023

© Higher Education Press 2024

ABSTRACT

Two-dimensional (2D) ferroelectric materials, which possess electrically switchable spontaneous polarization and can be easily integrated with semiconductor technologies, is of utmost importance in the advancement of high-integration low-power nanoelectronics. Despite the experimental discovery of certain 2D ferroelectric materials such as $CuInP_2S_6$ and In_2Se_3, achieving stable ferroelectricity at room temperature in these materials continues to present a significant challenge. Herein, stable ferroelectric order at room temperature in the 2D limit is demonstrated in van der Waals SnP_2S_6 atom layers, which can be fabricated via mechanical exfoliation of bulk SnP_2S_6 crystals. Switchable polarization is observed in thin SnP_2S_6 of ~7 nm. Importantly, a van der Waals ferroelectric field-effect transistor (Fe-FET) with ferroelectric SnP_2S_6 as top-gate insulator and p-type $WTe_{0.6}Se_{1.4}$ as the channel was designed and fabricated successfully, which exhibits a clear clockwise hysteresis loop in transfer characteristics, demonstrating ferroelectric properties of SnP_2S_6 atomic layers. In addition, a multilayer graphene/SnP_2S_6/multilayer graphene van der Waals vertical heterostructure phototransistor was also fabricated successfully, exhibiting improved optoelectronic performances with a responsivity (R) of 2.9 A/W and a detectivity (D) of 1.4×10^{12} Jones. Our results show that SnP_2S_6 is a promising 2D ferroelectric material for ferroelectric-integrated low-power 2D devices.

750 °C I$_2$ 700 °C
With
Reaction zone Growth zone
Sn+2P+6S $\xrightarrow[\Delta]{I_2}$ SnP_2S_6
2 mm
+2 V
−2 V
+2 V
0 200 pm 0 30 nm
V_d=0.1 V
Current (A)
V_g (V)

Keywords two-dimensional ferroelectric materials, ferroelectric field-effect transistors, photodetectors

1 Introduction

Ferroelectric materials possess stable and switchable spontaneous polarization attributes, rendering them suitable for deployment in diverse electronic devices, including sensors, memories, and piezoelectric components [1]. Nevertheless, the advancement of microelectronics technology necessitates the fabrication of low-power devices with higher density. The conventional perovskite ferroelectrics [2–4] encounter limitations due to depolarization fields [5, 6] and incongruity with the substrate lattice [7]. Hence, the advancement of two-dimensional ferroelectric layered materials presents a viable approach to address this unparalleled challenge. Primarily, the atomic-level thickness facilitates the utilization of two-dimensional

#Special Topic: Two-dimensional Electronic Materials and Devices (Eds.: Lin Wang & Xiaolong Chen).

Higher Education Press

https://doi.org/10.1007/s11467-023-1369-0

ferroelectric materials in the quest for enhanced integration and reduced power consumption. Additionally, a pristine van der Waals interface fosters the amalgamation of crystals and diverse substrates, emerging as a significant advantage for integration in semiconductor circuits [8]. Furthermore, the presence of a robust intralayer force and a relatively weaker interlayer force interaction suggests the potential for reduced interference from depolarization effects and the preservation of ferroelectricity at the atomic layer level. Additionally, the existence of distinctive dangling bonds, surface states, and the ability to withstand significant strain in two-dimensional (2D) materials offer significant advantages for the integration of two-dimensional ferroelectric materials with semiconductor technologies [9].

The theoretical anticipation of two-dimensional ferroelectric materials can be traced back to 2013 [10], effectively predicting potential candidates with inherent ferroelectricity, such as 1T-MoS_2 [11, 12], In_2Se_3 [13, 14], $CuInP_2S_6$ [15, 16], and MX (M = Ge, Sn, and X = S, Se, Te) [17–19]. The prediction of two-dimensional ferroelectricity is advantageous for the exploration of two-dimensional ferroelectric materials and their potential application in nano electronic devices. We have successfully synthesized a two-dimensional ferroelectric material, $CuInP_2S_6$, and observed switchable polarization in a thin film with a thickness of 4 nm at room temperature [20, 21]. However, the attribution of this phenomenon can be ascribed to the active Cu element, which poses challenges in achieving stable synthesis [15]. Furthermore, α-In_2Se_3 has been successfully fabricated as a ferroelectric controllable heterojunction, leading to a selective improvement in optical response [22, 23]. Despite the experimental discovery of certain 2D ferroelectric materials mentioned earlier, the achievement of stable ferroelectricity in 2D materials at room temperature remains a formidable obstacle.

As mentioned above, the experimental realization of two-dimensional room-temperature ferroelectric materials remains limited. Here, we report a novel 2D room-temperature ferroelectric material: SnP_2S_6 atomic layers, which can be prepared by the chemical vaper transport (CVT) growth of bulk SnP_2S_6 crystals and subsequent exfoliation bulk crystals into nanosheets. RT stable ferroelectric order can be achieved in 7 nm SnP_2S_6 atomic layers. The ferroelectric field effect transistor with SnP_2S_6 as the top gate insulator and $WTe_{0.6}Se_{1.4}$ as the channel material exhibits an obvious clockwise hysteresis loop, further identifying the ferroelectricity of SnP_2S_6. Furthermore, multilayer Graphene/SnP_2S_6/multilayer Graphene van der Waals vertical heterostructure phototransistor was successfully fabricated, possessing improved optoelectronic performances with responsivity (R) of 2.9 A/W and detectivity (D) of 1.4×10^{12} Jones. The experimental results have proven that SnP_2S_6 is an excellent 2D ferroelectric material, which is expected to provide new choices for low-power and highly integrated precision devices.

2 Experimental section

Sample preparation. Bulk SnP_2S_6 crystals were synthesized by the chemical vapor transport technique. At first, high pure Sn, P, and S powders (≥99.9%) with a molar ratio of 1:2:6 were mixed together (totally 0.5 g), and iodine was used as a transport agent. Then, they were sealed into a vacuum quartz tube (about 10^{-3} Pa) through high-temperature torch. Subsequently, the quartz tube was placed horizontally in a dual-temperature zone tubular furnace. The temperature of the source zone and growth zone were heated to 750 °C and 700 °C within 24 hours and kept at this temperature for 7 days so that the reaction could proceed completely. After heating, the quartz tube was naturally cooled to room temperature with the furnace. Finally, the plate-like SnP_2S_6 bulk crystals were successfully obtained after completing this growth process and 2D SnP_2S_6 flakes with various thicknesses were cleaved from the bulk crystals by mechanical exfoliation method.

XRD characterization. The powder X-ray diffraction patterns were collected using an X-ray diffractometer (D/MAX-2200, Rigaku) with monochromatized Cu-Karadiation at room temperature in the 2θ range of 10°–85° with a scan speed of 10(°)/min.

EDS characterization. Semi-quantitative microprobe analyses on the single crystals were performed with the aid of a field emission scanning electron microscope (Quanta 400 F, FEI) equipped with an energy dispersive X-ray spectroscope (EDS, Oxford INCA), which was applied to obtain semi-quantitative analysis results, like atomic ratio and elements dispersion mapping.

Optical characterization. SHG measurements were performed in reflection geometry with 100 fs pulses at 786 nm and a repetition rate of 76 MHz, which were focused to a spot size of ~1 μm by a 40 × 0.6 NA objective lens (Olympus). The PL spectra were recorded by a confocal microscope spectrometer (Alpha300 Raman, WITec). The optical absorption spectra were collected by a microscopic spectrophotometer (MSV-5200, Jasco).

Device fabrication. The devices were fabricated by laser direct imaging (μpg501, Heisenberg), and the corresponding Ti/Au (10 nm/100 nm) electrodes were deposited by electron beam evaporation (DE400, wavetest). (Opto)electronic measurements were performed under ambient conditions using a Keithley 4200 semiconductor parameter analyzer in a probe station. 405, 532, and 635 nm monochromatic lasers with tunable power were applied to investigate the photoresponse of SnP_2S_6.

AFM and PFM. Atomic force microscopy (AFM, Asylum Research Cypher S) in a tapping mode was used to characterize the morphology of the heterostructures and devices. The thickness of the SnP_2S_6 was identified by AFM. Out-of-plane PFM measurements were carried

out on the Cypher S AFM in the DART mode. Off-field PFM hysteresis loops were measured by recording the piezoresponse amplitude and phase signals after the individual DC pulse was turned off. P–E hysteresis loop measurements were carried out using a Radiant ferroelectric tester with an applied voltage of a triangular waveform at 1 kHz. Static transport properties were measured with an Agilent B1500A Semiconductor Device Parameter Analyzer in a vacuum chamber of 10^{-2} torr. The dynamic and writing speed tests were performed with the top-gate electrode connected to a RIGOL DG1032Z signal generator and source and drain connected to the Agilent B1500A.

TEM sample preparation and image simulations. The conventional wet-transfer method with the help of PMMA was used to transfer the exfoliated SnP_2S_6 flakes onto a Cu grid with a carbon film for preparation as a TEM sample. Z-contrast STEM imaging was carried out with a modified JEOL 2100F equipped with a delta probe corrector, which was used to correct for aberration up to the fifth order, resulting in a probe size of 1.4 Å. The imaging was conducted at an acceleration voltage of 60 kV. The convergent angle for illumination was ~35 mrad, with a collection detector angle ranging from 62 to 200 mrad.

3 Results and discussion

SnP_2S_6 crystallizes in a 2D atomic structure with C_3 point group and space group $R3$ (No. 146) [Figs. 1(a, b)] in which $a = b = 5.999$ Å, $c = 19.424$ Å, $\alpha = \beta = 90°$, $\gamma = 120°$, $V = 605.38$ Å^3, which was first reported in 1995 [24]. SnP_2S_6 exhibits a unique pore free structure as it lacks half of the metal ions compared to the parent $Sn_2P_2S_6$ structure [25, 26]. Due to its inherent 2D nanoporous structure, recent experimental studies have shown that SnP_2S_6 exhibits strong nonlinear optical response related to its inversion symmetry broken structure [25, 27]. It is worth noting that SnP_2S_6 monolayer consists of close-packed sulfur atomic skeleton, in which one third of vacancies with octahedral form are occupied by Sn (IV) ions in the form of $[SnS_6]^{8-}$, one third of vacancies are occupied by P–P pairs in the form of $[P_2S_6]^{4-}$ and the remaining ones are unoccupied. SnP_2S_6 bulk crystals was synthesized by the chemical vaper transport (CVT) method using iodine as a transport agent [Fig. 1(c)], see the Method Section for more details), which have a larger size than 5 mm and exhibit single-crystal morphologies, implying successful growth of high-quality single crystals [Fig. 1(d)]. The X-ray diffraction spectrum (XRD) of as-prepared SnP_2S_6 bulk crystals is in good agreement with standard PDF card (79818-icsd), suggesting high-purity phase of the as-prepared samples. Additionally, it is also noted that the XRD pattern of single-crystal SnP_2S_6 give strong peaks of $(000\bar{3})$, $(000\bar{6})$, $(000\bar{9})$, and $(000\overline{12})$, arising from the strong grain orientation along c axis [Fig. S1 of the Electronic Supplementary Materials (ESM)] [25]. To mitigate the impact of grain orientation on X-ray diffraction (XRD) analysis, the as-prepared SnP_2S_6 bulk crystals were pulverized into a fine powder. The resulting XRD pattern of the powder exhibits a satisfactory correspondence with the standard PDF card (79818-icsd) [Fig. 1(e)], wherein the intensity of four prominent grain-orientation peaks is diminished, while the emergence of peaks from alternative crystal planes is observed.

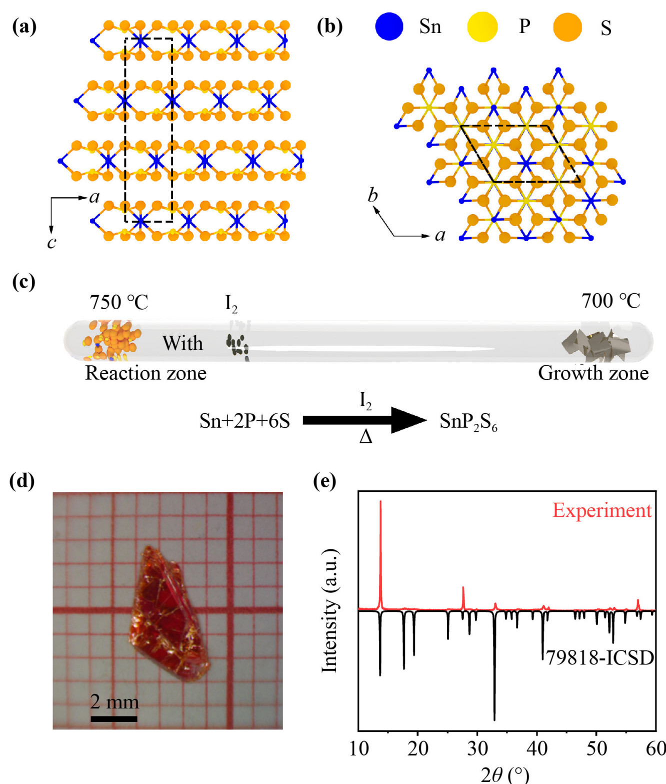

Fig. 1 Preparation and basic characterization of SnP_2S_6 crystal. **(a)** Crystal structure of SnP_2S_6 viewed along the b-axis and **(b)** the projection of the structure onto the (001) plane. Black dashed lines indicate unit cells. Blue sphere: Sn atoms; yellow sphere: P atoms; green sphere: S atoms. **(c)** Illustration of the growth of high-quality SnP_2S_6 single crystals from high-purity tin, phosphorus, and sulfur powders with iodine. **(d)** Optical image of high-quality SnP_2S_6 single crystal. **(e)** XRD patterns of SnP_2S_6 powder.

The layered structural behavior of SnP_2S_6 endows as-grown bulk crystals with sheet-like morphology with the c axis perpendicular to the surface plane of the sheets [Fig. 2(a)]. The energy dispersive X-ray spectrum (EDS) results show that the atomic ratio of Sn:P:S in as-grown bulk crystals is 0.97:2.03:5.99 [Fig. 2(a)], which is basically consistent with the stoichiometric ratio of 1:2:6, implying high qualities of as-grown bulk crystals. The atomic structure was further characterized and proven to be consistent with the atoms in the a–b plane by scanning transmission electron microscopy (STEM) image [Fig. 1(b) and Fig. S2 of the ESM]. SnP_2S_6 atomic layers

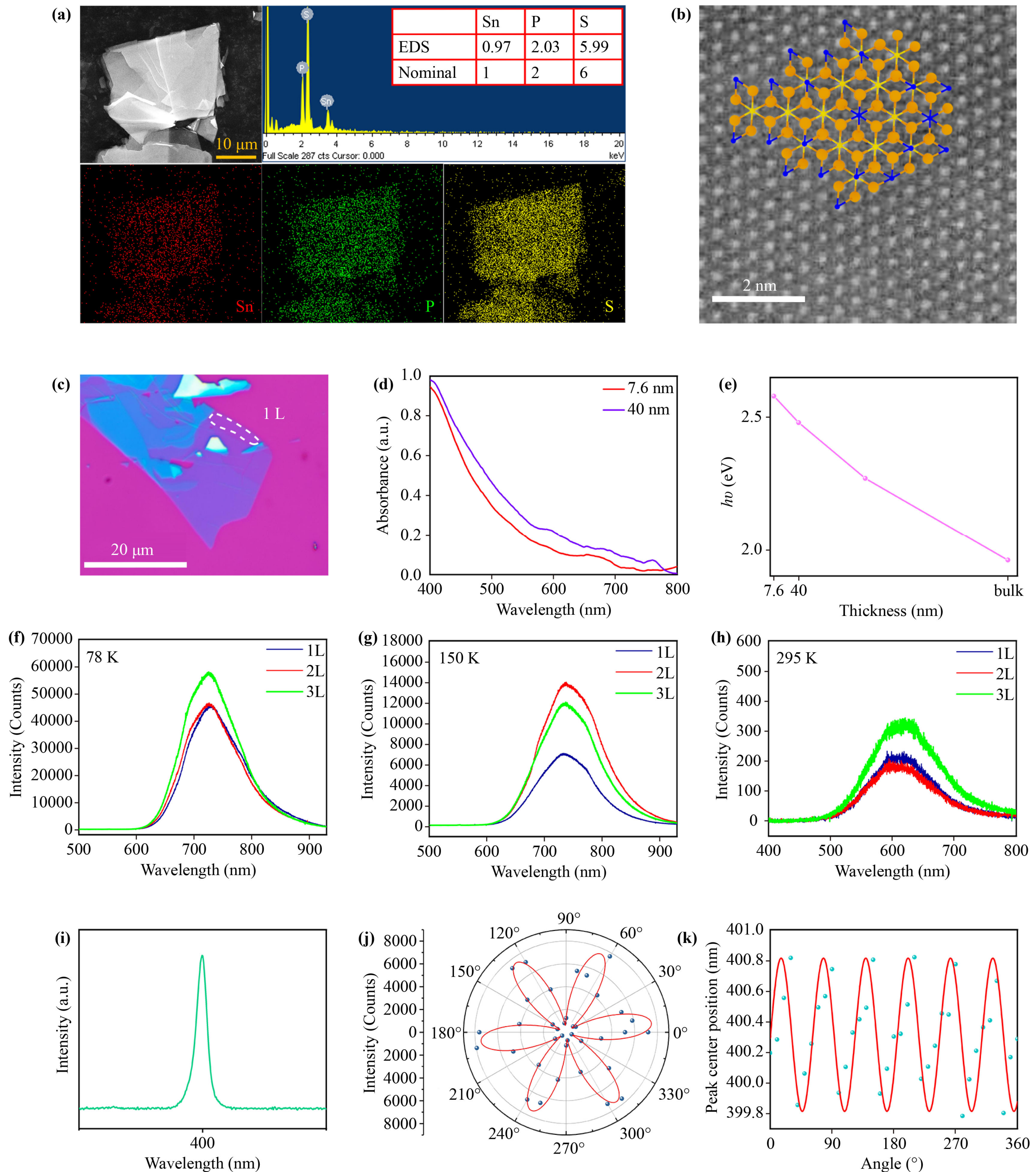

Fig. 2 Characterization of SnP_2S_6 thin film. **(a)** The EDS analysis and the atomic ratio result. Upper left panel: Scanning electron microscopy (SEM) image for SnP_2S_6 thin film. Upper right panel: The EDS analysis and the atomic ratio result. Lower panel: EDS elemental mapping of the upper left panel. **(b)** STEM image and matched crystal structures of SnP_2S_6. Blue sphere: Sn atoms; yellow sphere: P atoms; green sphere: S atoms. **(c)** Optical images of exfoliated SnP_2S_6 large area thin films, the area within the dashed line is a single atomic layer. **(d)** UV–Vis–NIR absorption spectrum of SnP_2S_6. **(e)** Absorption bandgap as a function of thickness. **(f–h)** PL spectra of 1–3L at 78 K (f), 150 K (g) and 295 K (h). **(i)** SHG under 800 nm wavelength laser. **(j)** Polar plots of the SHG intensity as a function of the excitation laser linear polarization. **(k)** Peak center position as a function of the excitation laser linear polarization.

with thickness gradient were prepared on SiO_2/Si (100) substrate via mechanical exfoliation method [28], in which the size of the monolayer with uniform thickness can reach 13 μm [Fig. 2(c)]. Micro-regions UV–Vis–NIR absorption spectrum is used to measure the bandgaps of SnP_2S_6 atomic layers, in which the absorption of SnP_2S_6 decreases with decreasing thicknesses [Fig. 2(d)] as well as the bandgaps can be changed from 1.96 eV (bulk sample) to 2.58 eV (7.6 nm nanosheets) [Fig. 2(e)]. In order to evaluate the interlayer interaction of SnP_2S_6, photoluminescence spectra (PL) of SnP_2S_6 atomic layers at different temperatures were measured [Figs. 2(f)–(h)], in which the PL peaks of the trilayer, bilayer and monolayer are located between 715 nm and 735 nm, basically consistent with the previous reports [29]. Additionally, under the conditions of 78 K and 150 K, PL peaks can be observed at 725 nm and 735 nm, respectively, indicating that the band gap of thin-layer SnP_2S_6 decreases with increasing temperature. It is also worth noting that as the thickness decreases, the intensity of the PL peak also decreases, which is consistent with the absorption peak mentioned earlier. Second nonlinear optical characterizations of SnP_2S_6 were performed to identify the noncentrosymmetric structure of SnP_2S_6. Under the excitation of 800 nm laser, a second harmonic generation (SHG) signal with 400 nm was stably generated, further confirming the breaking inversion symmetry of as-prepared SnP_2S_6 [Fig. 2(i)]. Interestingly, the resulting polarization of SHG intensities displays the six-fold rotational symmetry [Figs. 2(j, k)], identifying that as-grown samples belong to the C_3 point group with broken inversion symmetry [30, 31]. In addition, the Raman spectra of bulk SnP_2S_6 were also measured, in which there were three obvious Raman peaks identified as P_1 (140 cm^{-1}), P_2 (166 cm^{-1}), and P_3 (266 cm^{-1}), consistent with previous reports [25]. It is found that, for few-layer SnP_2S_6, only weakened P_3 peak can be observed and no P_1 and P_2 peaks can be found (Fig. S3 of the ESM), which is also observed in previous reports [25]. Such weak Raman intensities can be attributed to weak optical absorption of few-layer SnP_2S_6.

In order to explore the ferroelectricity of SnP_2S_6 thin films, the atomic force microscope (AFM) and piezoresponse force microscope (PFM) tests were carried out on the exfoliated SnP_2S_6 few layers (see the Method Section for details). A 15-nm-thick SnP_2S_6 nanosheet [Fig. 3(a)] was fabricated via mechanical exfoliation method to study its ferroelectricity, which possesses good uniformity in thickness [Fig. 3(d)], making it an ideal sample to eliminate the interference of surface fluctuations on piezoelectric response force at the nanoscale. There are dendritic and partially black dot patterns in both PFM amplitude [Fig. 3(b)] and PFM phase [Fig. 3(c)], where PFM amplitude reflects the modulus of local piezoelectric response and phase reflects the polarization direction of each region. The values of amplitude [Fig. 3(e)] and phase [Fig. 3(f)] are extracted from the same position of the film, indicating their good consistency. The PFM signals obtained from the clean surface indicates the existence of spontaneous polarized ferroelectric domains on the film, which is the direct evidence of the ferroelectricity of SnP_2S_6 at room temperature. Examples of more ferroelectric domains in SnP_2S_6 with different thicknesses are given in Fig. S4 of the ESM. Although the ferroelectricity of layered SnP_2S_6 has been proven, the switchable polarization of ferroelectrics also needs to be proven because some effects, such as depolarization effect [32], interface pinning effect [33], and "dead layer" effect [34] on thin films, will lead to the absence of the ferroelectricity. The desired pattern was obtained in the PFM test by applying voltage between the conductive tip and the substrate. For a flat sheet [Fig. 3(g)] with a thickness of 7 nm (Fig. S5 of the ESM), a DC voltage of +2 V, –2 V and +2 V is applied from the outside to the inside. The clearly layered rectangular amplitude pattern shows that SnP_2S_6 nanosheet has controllable spontaneous polarization property [Fig. 3(h) and Fig. S6 of the ESM]. In addition, the clear ferroelectric hysteresis loops were also observed on the phase diagram and amplitude diagram [Fig. 3(i)], further demonstrating the switchable spontaneous polarization of SnP_2S_6 as a ferroelectric material.

Despite SnP_2S_6 as an ultra-thin ferroelectric material has been demonstrated by PFM tests, only one way to identify the RM ferroelectricity is inadequate. Therefore, a ferroelectric field-effect transistor (Fe-FET), with SnP_2S_6 atomic layers as the top ferrielectric gate, thin h-BN layer as the top gate insulator, and p-type semiconductor $WTe_{0.6}Se_{1.4}$ as a channel material at the bottom [Fig. 4(a)], was fabricated to further confirm the RM ferroelectricity of SnP_2S_6, in which the introduction of h-BN effectively improves the interface contact performance and prevents gate current breakdown [35, 36]. In addition, graphene is used to connect the channel with the metal electrodes, which, indeed, also act as the electrodes. Figure 4(b) shows an optical image of as-fabricated ferroelectric transistor, from which it can be clearly seen that the gate completely covers the channel material.

The output curve of the Fe-FET was measured at room temperature with a top-gate V_g varying from –0.6 V to 0.6 V at a step of 0.2 V [Fig. 4(c)], which are almost straight, indicating that the device has good ohmic contact. When the top-gate voltages as a floating gate are changed from 0.5 V to –0.5 V, then –0.5 V to 0.5 V, the Fe-FET exhibit a clear clockwise hysteresis loop in transfer characteristics, also demonstrating ferroelectric properties of SnP_2S_6. Meanwhile, it is worth noting that a small change of V_g leads to the change of drain current, revealing that, in SnP_2S_6-based Fe-FET, the ferroelectric state switching is easy and can work under low power consumption. Moreover, the transfer curve of Fe-FET shows typical p-type semiconductor characteristics of few-layer $WTe_{0.6}Se_{1.4}$, in which the ferroelectric resistance switching can realizes more than two orders of magnitude changes [Fig. 4(d)]. The switching

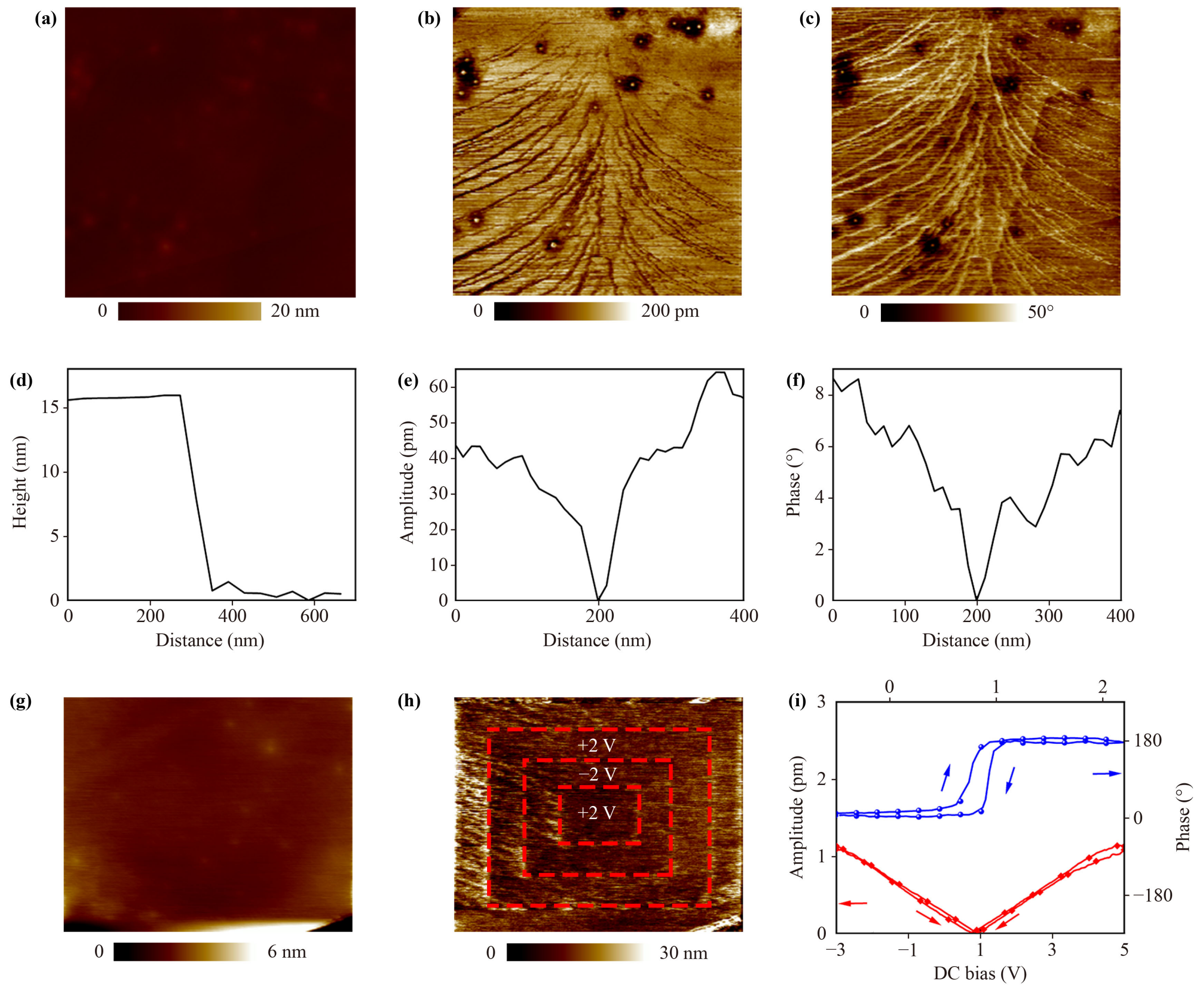

Fig. 3 Atomic force microscope (AFM) and piezoresponse force microscope (PFM) characterozations of SnP_2S_6. **(a–c)** AFM topography (a) PFM amplitude (b) and PFM phase (c) of a SnP_2S_6 thin film at room temperature. **(d)** Height of the thin film for (a). **(e)** PFM amplitude and **(f)** PFM phase measurement of ferroelectric domains in thin films. **(g)** AFM topography for 7 nm SnP_2S_6 thin film. **(h)** PFM phase images of thin film for (g) with written box-in-box patterns at room temperature with reverse DC bias of +2 V, −2 V and +2 V. **(i)** The corresponding PFM amplitude and phase hysteresis loops during the switching process for 7 nm SnP_2S_6 thin film.

of the state comes from the switching of ferroelectric polarization, which changes the carrier of the channel material [37]. When the Fe-FET is applied in a negative top-gate voltage, the valence band edge (E_V) will bend above the Fermi level (E_F) of the p-type semiconductor, leading to the generation of holes and the formation of low channel resistance states (LRS) in the semiconductor layer. On the contrary, the positive V_g will lead to the generation of moving electrons due to the occurrence of polarization transformation, further cause the generation of high channel resistance states (HRS). Therefore, owning to the existence of residual polarization, the channel resistances will have a clockwise hysteresis loop under a floating gate. The characterizations of Fe-FET identify that SnP_2S_6 is a novel 2D ferroelectric material again, which can be used in nonvolatile memory device.

To investigate the optoelectronic properties of SnP_2S_6 thin film, a parallel photodetector based on 75 nm SnP_2S_6 nanosheet was prepared [Fig. 5(a)], which was excited by a 405 nm laser (with a spot diameter of 1 cm, much larger than the size of the device). The output curve of the parallel phototransistor transistor [Fig. 5(b)] exhibits a quasi-Ohmic contact, and the photocurrent is related to the power density of the laser. Under 405 nm laser irradiation, the photocurrent tends to saturate with increasing light power density. In order to further evaluate the performances of the device, responsivity (R) and detectivity (D) are introduced. The responsivity is

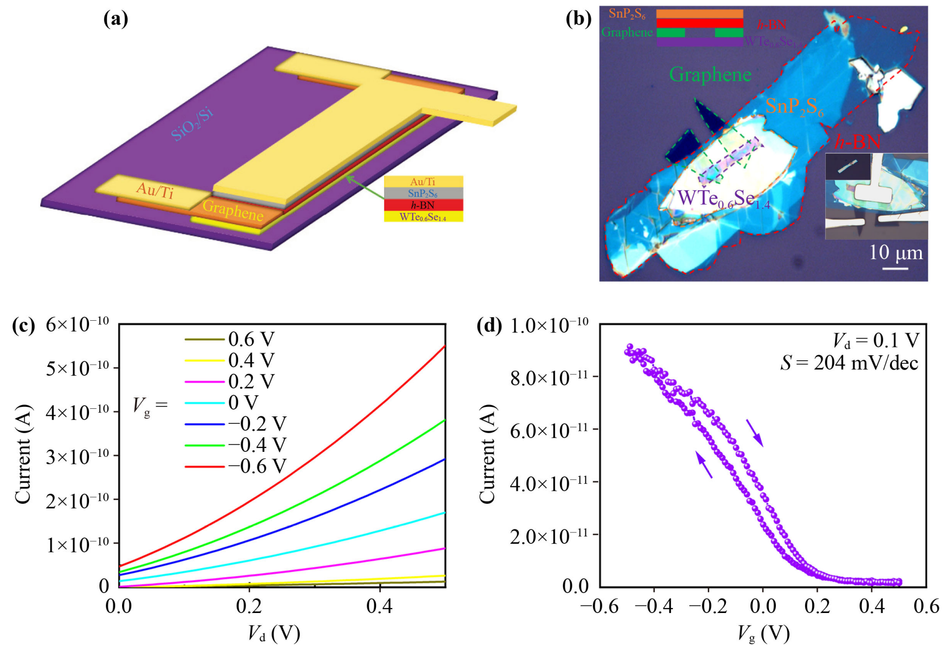

Fig. 4 A $SnP_2S_6/WTe_{0.6}Se_{1.4}$ van der Waals ferroelectric field-effect transistor (Fe-FET). **(a)** Schematic diagram of the Fe-FET. Few-layer $WTe_{0.6}Se_{1.4}$ is applied as the channel material. The top-gate stack consists of CIPS as the ferroelectric gate insulator and h-BN as the gate insulator. Few-layer graphene and Ni/Au act as the gate electrodes. **(b)** Top-view optical image of 2D heterostructure, the inset is top-view image of as-fabricated device. **(c)** Output curves for different gate voltages at room temperature. **(d)** Top-gate transfer curves of the Fe-FET measured at room temperature with a floating gate (scanning from 0.5 V to –0.5 V, then –0.5 V to 0.5 V).

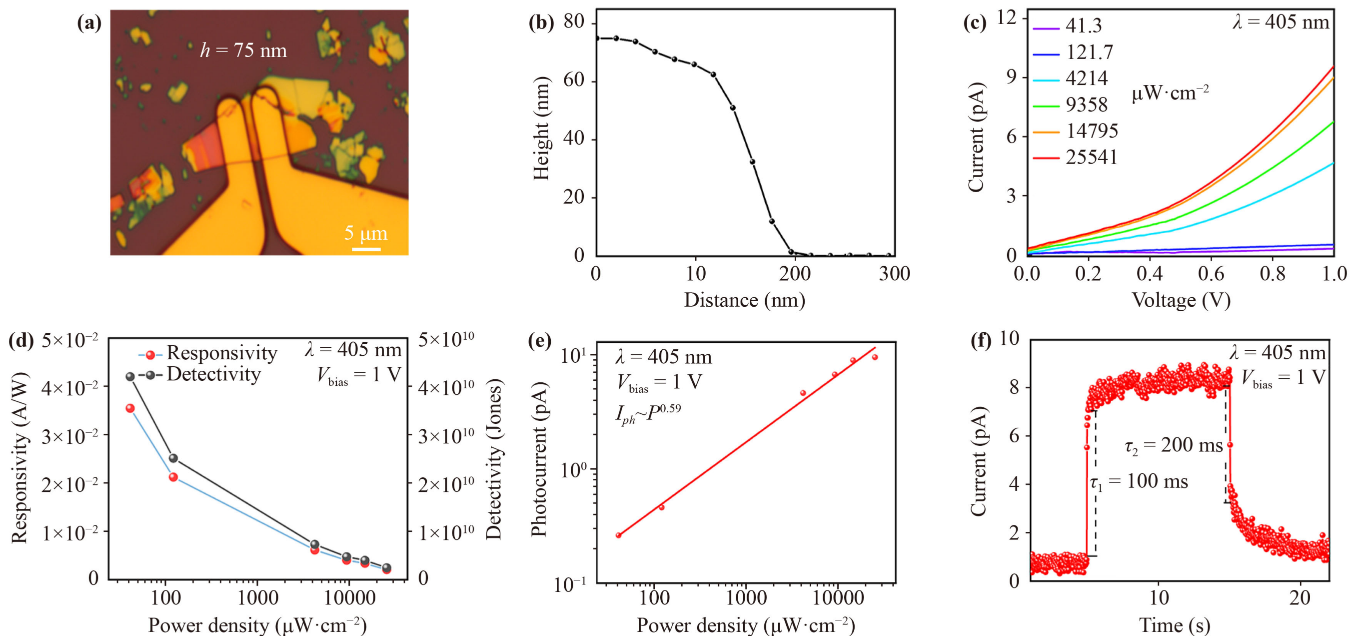

Fig. 5 Optoelelctronic characterization of SnP_2S_6 parallel phototransistor under 405 nm laser. **(a)** Top-view optical image of the SnP_2S_6 parallel phototransistor, height of SnP_2S_6 thin film is 75 nm. The active channel area of parallel phototransistor is 1.79×10^{-7} cm^2. **(b)** The AFM characterization of thin film shown in (a). **(c)** Output curves for different light power densities at temperature. **(d)** Responsivity and detectivity as functions of light power density for $V_{\text{bias}} = 1$ V at room temperature. **(e)** Photocurrent dependent on light power density at room temperature, where the light power density is on the logarithmic coordinate axis. **(f)** Time-resolved photoresponse of the parallel transistors at $V_{\text{bias}} = 1$ V under laser (λ = 405 nm) illumination, the rise time τ_1 is 100 ms and the decay time τ_2 is 200 ms.

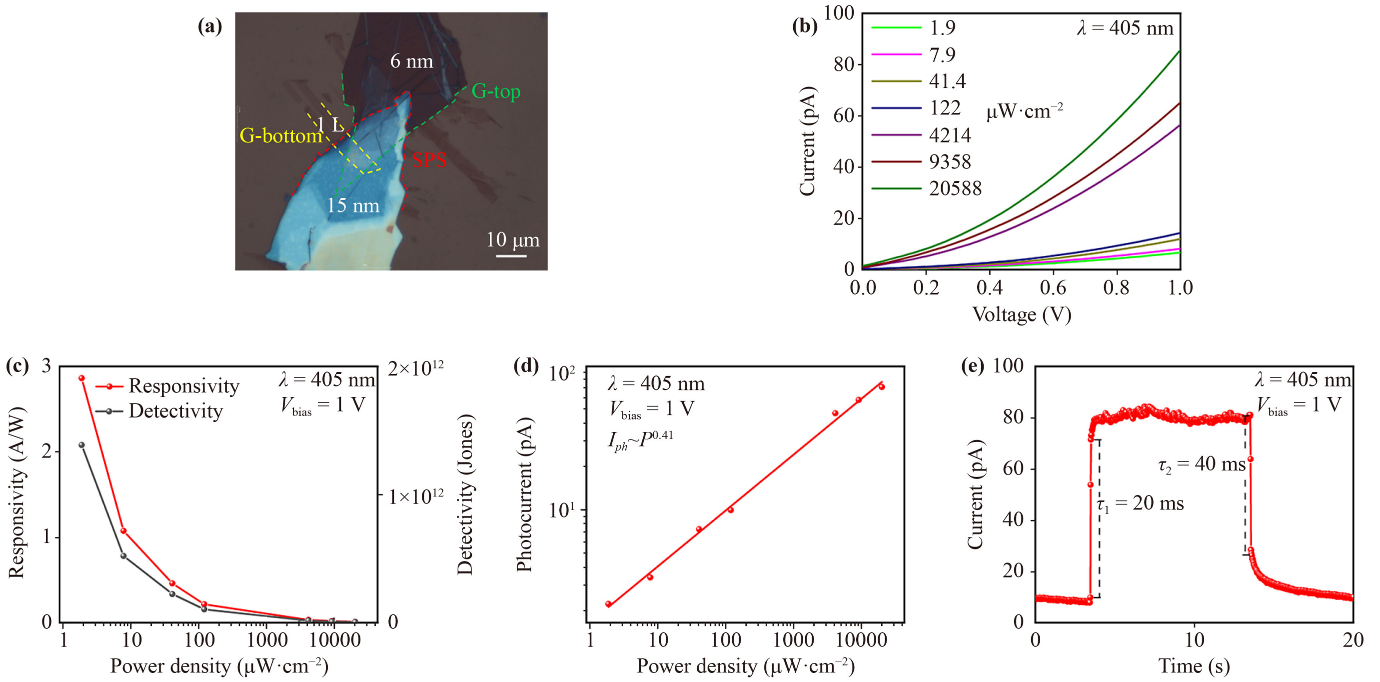

Fig. 6 Optoelelctronic characterization of SnP_2S_6 vertical transistor under 405 nm laser. **(a)** Top-view optical image of the vertical transistor. Yellow area of G-bottom is single layer bottom graphene, green area of G-top is top graphene with a thickness of 6 nm, and red area of SPS is few-layer SnP_2S_6 with a thickness of 15 nm. The active channel area of vertical transistor is 3.77×10^{-7} cm^2. **(b)** Output curves for different light power densities at temperature. **(c)** Responsivity and detectivity as functions of light power density for $V_{\rm bias} = 1$ V at room temperature. **(d)** Photocurrent dependent on light power density at room temperature, where the light power density is on the logarithmic coordinate axis. **(e)** Time-resolved photoresponse of the parallel transistors at $V_{\rm bias} = 1$ V under laser ($\lambda = 405$ nm) illumination, the rise time τ_1 is 20 ms and the decay time τ_2 is 40 ms.

defined by $R = I_{\rm ph}/(PS)$, where $I_{\rm ph}$ is photocurrent ($I_{\rm ph} = I_{\rm light} - I_{\rm dark}$), P is light power density, S is active channel area, $I_{\rm light}$ and $I_{\rm dark}$ are the drain currents under light and dark. Detectivity is a powerful parameter for comparing the capability to detect weak light signal of photodetectors with various geometries. It is defined as $D = RS^{1/2}/(2qI_{\rm dark})^{1/2}$, where R is the responsivity, S is the effective area of the device, and $I_{\rm dark}$ is the dark current. The parallel device shows a photoresponsivity (R) of 3.6×10^{-2} A/W and a detectivity (D) of 4.2×10^{10} Jones at a light power density of 41.3 μW·cm^{-2} and a bias voltage of 2 V. Additionally, it was also observed that the R and D decrease with increasing power densities of the lasers [Fig. 5(c)], attributed to severe frequent carrier recombination and shorter carrier lifetime at stronger illumination. The value of α, extracted from $I_{\rm ph} \propto P^{\alpha}$, is introduced to judge the mechanism of photocurrent generation, where $I_{\rm ph}$ is drain current under light and P is light power density [38]. The factor α of 0.59 is achieved in our parallel photodetector, which is smaller than 1, indicating that the recombination kinetics of photocarriers involves both trap states and interactions between photogenerated carriers [39], and it may have a certain impact on the reaction speed of the device. Generally, the rise time and the decay time are used to evaluate the response speed of devices, fitted by the following equation: $I_{\rm rise} = I_0 - A\exp(-(t - t_1)/\tau_1)$ and $I_{\rm decay} = I_0 - B\exp(-(t - t_2)/\tau_2)$, where τ is the time constant, t is the time when laser is switched on or off, and A and B are the scaling constants. Therefore, the fitted characteristic photoresponse time coefficients, τ_1 and τ_2, are 100 ms and 200 ms, respectively. It is worth noting that the rise time is faster than the decay time because the photocarriers can be trapped in the trap states to further result in an increase in the lifetime [40–43]. In addition, the optoelectronic performances of our parallel device is also assessed under illumination of 532-nm and 635-nm lasers, in which the photoresponsivities and the rise times are 2.7×10^{-3} A/W and 260 ms for the former [Fig. S7(b) of the ESM], 1.4×10^{-3} A/W and 2 s for the latter [Fig. S7(c) of the ESM], respectively. The poor optoelectronic performances under 532-nm and 635-nm lasers should be attributed to the poor optical absorption.

Based on our previous reports that fully vertical van der Waals heterostructure photodetector can efficiently improve the optoelectronic performances, fully vertical van der Waals heterostructure photodetector of $CuBiP_2Se_6$ [44], a multilayer graphene/SnP_2S_6/multilayer graphene van der Waals vertical heterostructure phototransistor, was fabricated with 15 nm channel width [Fig. 6(a)]. Photoresponse is observed at a low light

power density of 1.9 μW·cm^{-2} and a stronger photocurrent was exhibited [Fig. 6(b)]. It is worth noting that the great improved R of 2.9 A/W and D of 1.4 × 10^{12} Jones are achieved because the short channel effect of our vertical device efficiently reduces the scattering of photocarriers in the channel [45, 46]. The α of 0.41 indicates that vertical devices also do not change the influence of their intrinsic trap states on photogenerated charge carriers [Fig. 6(d)]. The rise time of vertical device is significantly improved to 20 ms due to the introduction of heterojunctions and nanoscale channel length. However, the improved decay time of 40 ms is still longer than the rise time because of its intrinsic recombination kinetics. Furthermore, the optoelectronic performances of our vertical device are also performed under illumination of 532-nm and 635-nm lasers, in which the photoresponsivities and the rise times are 0.02 A/W and 200 ms for the former [Fig. S8(b) of the ESM], 0.0015 A/W and 300 ms for the latter [Fig. S7(c) of the ESM], respectively. As in the parallel device, the poor optoelectronic performances of the vertical device under 532-nm and 635-nm lasers should be also attributed to the poor optical absorption.

4 Conclusion

In this work, we developed a novel two-dimensional ferroelectric material, van der Waals SnP_2S_6, with room-temperature ferroelectricity in ~7 nm thick flake. A Fe-FET with ferroelectric SnP_2S_6 was designed and fabricated successfully, which exhibits a clear clockwise hysteresis loop in transfer characteristics, and the ferroelectric behavior has the potential to be applied to non-volatile storage device. Meanwhile, we also designed and fabricated a multilayer graphene/SnP_2S_6/multilayer graphene van der Waals vertical heterostructure phototransistor with improved R of 2.9 A/W and D of 1.4 × 10^{12} Jones. 2D ferroelectric SnP_2S_6, with its ability to integrate with mature silicon-based platforms, enriches the family of ferroelectric materials and the functionality of two-dimensional materials, making it an excellent candidate for the next generation of nano-electronic devices.

Declarations The authors declare that they have no competing interests and there are no conflicts.

Electronic supplementary materials The online version contains supplementary material available at https://doi.org/10.1007/s11467-023-1369-0 and https://journal.hep.com.cn/fop/EN/10.1007/s11467-023-1369-0.

Acknowledgements This work was supported by the National Key Research and Development Program of China (Nos. 2021YFE0194200 and 2021YFA1200903), the National Natural Science Foundation of China (No. 22175203), the Natural Science Foundation of Guangdong Province (Nos. 2022B1515020065 and 2020A1515110821), and the Guangzhou Science and Technology Project (No. 202102020126). This work was also supported by the Plan Fostering Project of State Key Laboratory of Optoelectronic Materials and Technologies, of Sun Yat-sen University (No. OEMT-2021-PZ-02).

References

1. G. D. Wenbiao Niu, Z. Jia, X. Q. Ma, J. Y. Zhao, K. Zhou, S. T. Han, C. C. Kuo, and Y. Zhou, Recent advances in memristors based on two-dimensional ferroelectric materials, *Front. Phys.* 19(1), 13402 (2024)
2. T. Sano, Y. Nishio, Y. Hamada, H. Takahashi, T. Usuki, and K. Shibata, Design of conjugated molecular materials for optoelectronics, *J. Mater. Chem.* 10(1), 157 (2000)
3. I. B. Bersuker, I. Y. Ogurtsov, and Y. V. Shaparev, Temperature dependence of the mean dipole moment of symmetrical molecular systems, *Theor. Exp. Chem.* 9(4), 351 (1975)
4. P. Li, Z. M. Gao, X. S. Huang, L. F. Wang, W. F. Zhang, and H. Z. Guo, Ferroelectric polarization reversal tuned by magnetic field in a ferroelectric $BiFeO_3$/Nb-doped $SrTiO_3$ heterojunction, *Front. Phys.* 13, 136803 (2018)
5. J. M. D. Coey, M. Venkatesan, P. Stamenov, C. B. Fitzgerald, and L. S. Dorneles, Magnetism in hafnium dioxide, *Phys. Rev. B* 72(2), 024450 (2005)
6. D. E. Aspnes, Electric field effects on the dielectric constant of solids, *Phys. Rev.* 153(3), 972 (1967)
7. D. G. Schlom, L. Q. Chen, C. B. Eom, K. M. Rabe, S. K. Streiffer, and J. M. Triscone, Strain tuning of ferroelectric thin films, *Annu. Rev. Mater. Res.* 37(1), 589 (2007)
8. M. H. Wu, Two-dimensional van der Waals ferroelectrics: Scientific and technological opportunities, *ACS Nano* 15(6), 9229 (2021)
9. Y. Liu, Y. Huang, and X. F. Duan, Van der Waals integration before and beyond two-dimensional materials, *Nature* 567(7748), 323 (2019)
10. M. H. Wu, J. D. Burton, E. Y. Tsymbal, X. C. Zeng, and P. Jena, Hydroxyl-decorated graphene systems as candidates for organic metal-free ferroelectrics, multiferroics, and high-performance proton battery cathode materials, *Phys. Rev. B* 87(8), 081406 (2013)
11. S. G. Yuan, X. Luo, H. L. Chan, C. C. Xiao, Y. W. Dai, M. H. Xie, and J. H. Hao, Room-temperature ferroelectricity in $MoTe_2$ down to the atomic monolayer limit, *Nat. Commun.* 10(1), 1775 (2019)
12. S. N. Shirodkar and U. V. Waghmare, Emergence of ferroelectricity at a metal-semiconductor transition in a 1T monolayer of MoS_2, *Phys. Rev. Lett.* 112(15), 157601 (2014)
13. C. X. Zheng, L. Yu, L. Zhu, J. L. Collins, D. Kim, Y. D. Lou, C. Xu, M. Li, Z. Wei, Y. P. Zhang, M. T. Edmonds, S. Q. Li, J. Seidel, Y. Zhu, J. Z. Liu, W. X. Tang, and M. S. Fuhrer, Room temperature in-plane ferroelectricity in van der Waals In_2Se_3, *Sci. Adv.* 4(7), eaar7720 (2018)
14. W. J. Ding, J. B. Zhu, Z. Wang, Y. F. Gao, D. Xiao, Y. Gu, Z. Y. Zhang, and W. G. Zhu, Prediction of intrinsic two-dimensional ferroelectrics in In_2Se_3 and other

III_2–VI_3 van der Waals materials, *Nat. Commun.* 8(1), 14956 (2017)
15. F. C. Liu, L. You, K. L. Seyler, X. B. Li, P. Yu, J. H. Lin, X. W. Wang, J. D. Zhou, H. Wang, H. Y. He, S. T. Pantelides, W. Zhou, P. Sharma, X. D. Xu, P. M. Ajayan, J. L. Wang, and Z. Liu, Room-temperature ferroelectricity in $CuInP_2S_6$ ultrathin flakes, *Nat. Commun.* 7, 12357 (2016)
16. A. Belianinov, Q. He, A. Dziaugys, P. Maksymovych, E. Eliseev, A. Borisevich, A. Morozovska, J. Banys, Y. Vysochanskii, and S. V. Kalinin, $CuInP_2S_6$ room temperature layered ferroelectric, *Nano Lett.* 15(6), 3808 (2015)
17. P. Z. Hanakata, A. Carvalho, D. K. Campbell, and H. S. Park, Polarization and valley switching in monolayer group-IV monochalcogenides, *Phys. Rev. B* 94(3), 035304 (2016)
18. R. X. Fei, W. Kang, and L. Yang, Ferroelectricity and phase transitions in monolayer group-IV monochalcogenides, *Phys. Rev. Lett.* 117(9), 097601 (2016)
19. F. Alsubaie, M. Muraykhan, L. Zhang, D. C. Qi, T. Liao, L. Z. Kou, A. J. Du, and C. Tang, Two-dimensional polarized MoSSe/$MoTe_2$ van der Waals heterostructure: A polarization-tunable optoelectronic material, *Front. Phys.* 19(1), 13201 (2024)
20. L. Y. Shuang Zhou, H. Zhou, Y. Pu, Z. Gui, and J. Wang, Van der Waals layered ferroelectric $CuInP_2S_6$: Physical properties and device applications, *Front. Phys.* 16(1), 13301 (2021)
21. L. Niu, F. C. Liu, Q. S. Zeng, X. Y. Zhu, Y. L. Wang, P. Yu, J. Shi, J. H. Lin, J. D. Zhou, Q. D. Fu, W. Zhou, T. Yu, X. F. Liu, and Z. Liu, Controlled synthesis and room-temperature pyroelectricity of $CuInP_2S_6$ ultrathin flakes, *Nano Energy* 58, 596 (2019)
22. J. Wang, C. L. Liu, L. B. Zhang, J. Chen, J. Chen, F. L. Yu, Z. Y. Zhao, W. W. Tang, X. Li, S. Zhang, G. H. Li, L. Wang, Y. Cheng, and X. S. Chen, Selective enhancement of photoresponse with ferroelectric-controlled BP/In_2Se_3 vdW heterojunction, *Adv. Sci. (Weinh.)* 10(11), 2205813 (2023)
23. Y. Cai, J. Yang, F. Wang, S. Li, Y. Wang, X. Zhan, F. Wang, R. Cheng, Z. Wang, and J. He, Ultrasensitive solar-blind ultraviolet detection and optoelectronic neuromorphic computing using α-In_2Se_3 phototransistors, *Front. Phys.* 18(3), 33308 (2023)
24. Q. Liang, Y. Zheng, C. Du, Y. Luo, J. Zhao, H. Ren, J. Xu, and Q. Yan, Asymmetric-layered tin thiophosphate: An emerging 2D ternary anode for high-performance sodium ion full cell, *ACS Nano* 12(12), 12902 (2018)
25. Y. Zhang, F. K. Wang, X. Feng, Z. D. Sun, J. W. Su, M. Zhao, S. Z. Wang, X. Z. Hu, and T. Y. Zhai, Inversion symmetry broken 2D SnP_2S_6 with strong nonlinear optical response, *Nano Res.* 15(3), 2391 (2022)
26. Z. Wang, R. D. Willett, R. A. Laitinen, and D. A. Cleary, Synthesis and crystal structure of SnP_2S_6, *Chem. Mater.* 7(5), 856 (1995)
27. I. P. Studenyak, V. V. Mitrovcij, G. S. Kovacs, O. A. Mykajlo, M. I. Gurzan, and Y. M. Vysochanskii, Temperature variation of optical absorption edge in $Sn_2P_2S_6$ and SnP_2S_6 crystals, *Ferroelectrics* 254(1), 295 (2001)
28. K. S. Novoselov, A. K. Geim, S. V. Morozov, D. Jiang, Y. Zhang, S. V. Dubonos, I. V. Grigorieva, and A. A. Firsov, Electric field effect in atomically thin carbon films, *Science* 306(5696), 666 (2004)
29. Y. Zhang, F. K. Wang, X. Feng, Z. Zhang, K. L. Liu, F. F. Xia, W. X. Liang, X. Z. Hu, Y. Ma, H. Q. Li, G. C. Xing, and T. Y. Zhai, Self-trapped excitons in 2D SnP_2S_6 crystal with intrinsic structural distortion, *Adv. Funct. Mater.* 32(38), 2205757 (2022)
30. J. Y. He, S. H. Lee, F. Naccarato, G. Brunin, R. Zu, Y. X. Wang, L. X. Miao, H. Y. Wang, N. Alem, G. Hautier, G. M. Rignanese, Z. Q. Mao, and V. Gopalan, SnP_2S_6: A promising infrared nonlinear optical crystal with strongnonresonant second harmonic generation and phase-matchability, *ACS Photonics* 9(5), 1724 (2022)
31. X. Bourdon and V. B. Cajipe, Soft-chemistry forms of $Sn_2P_2S_6$ and $CuInP_2S_6$, *J. Solid State Chem.* 141(1), 290 (1998)
32. S. S. Cheema, D. Kwon, N. Shanker, R. dos Reis, S. L. Hsu, J. Xiao, H. Zhang, R. Wagner, A. Datar, M. R. McCarter, C. R. Serrao, A. K. Yadav, G. Karbasian, C. H. Hsu, A. J. Tan, L. C. Wang, V. Thakare, X. Zhang, A. Mehta, E. Karapetrova, R. V. Chopdekar, P. Shafer, E. Arenholz, C. Hu, R. Proksch, R. Ramesh, J. Ciston, and S. Salahuddin, Enhanced ferroelectricity in ultrathin films grown directly on silicon, *Nature* 580(7804), 478 (2020)
33. M. G. Han, M. S. J. Marshall, L. J. Wu, M. A. Schofield, T. Aoki, R. Twesten, J. Hoffman, F. J. Walker, C. H. Ahn, and Y. M. Zhu, Interface-induced nonswitchable domains in ferroelectric thin films, *Nat. Commun.* 5(1), 4693 (2014)
34. M. Stengel and N. A. Spaldin, Origin of the dielectric dead layer in nanoscale capacitors, *Nature* 443(7112), 679 (2006)
35. E. Tokumitsu, K. Okamoto, and H. Ishiwara, Low voltage operation of nonvolatile metal–ferroelectric–metal–insulator–semiconductor (MFMIS)-field-effect-transistors (FETs) using $Pt/SrBi_2Ta_2O_9/Pt/SrTa_2O_6/SiON/Si$ structures, *Jpn. J. Appl. Phys.* 40(4S), 2917 (2001)
36. J. M. Xue, J. Sanchez-Yamagishi, D. Bulmash, P. Jacquod, A. Deshpande, K. Watanabe, T. Taniguchi, P. Jarillo-Herrero, and B. J. Leroy, Scanning tunnelling microscopy and spectroscopy of ultra-flat graphene on hexagonal boron nitride, *Nat. Mater.* 10(4), 282 (2011)
37. C. Wang, K. J. Jin, Z. T. Xu, L. Wang, C. Ge, H. B. Lu, H. Z. Guo, M. He, and G. Z. Yang, Switchable diode effect and ferroelectric resistive switching in epitaxial $BiFeO_3$ thin films, *Appl. Phys. Lett.* 98(19), 192901 (2011)
38. J. O. Island, S. I. Blanter, M. Buscema, H. S. J. van der Zant, and A. Castellanos-Gomez, Gate controlled photocurrent generation mechanisms in high-gain In_2Se_3 phototransistors, *Nano Lett.* 15(12), 7853 (2015)
39. H. H. Fang and W. D. Hu, Photogating in low dimensional photodetectors, *Adv. Sci. (Weinh.)* 4(12), 1700323 (2017)
40. P. Yu, Q. S. Zeng, C. Zhu, L. J. Zhou, W. N. Zhao, J. C. Tong, Z. Liu, and G. W. Yang, Ternary Ta_2PdS_6 atomic layers for an ultrahigh broadband photoresponsive phototransistor, *Adv. Mater.* 33(2), 2005607 (2021)

41. Q. J. Liang, Q. X. Wang, Q. Zhang, J. X. Wei, S. X. D. Lim, R. Zhu, J. X. Hu, W. Wei, C. Lee, C. Sow, W. J. Zhang, and A. T. S. Wee, High-performance, room temperature, ultra-broadband photodetectors based on air-stable $PdSe_2$, *Adv. Mater.* 31(24), 1807609 (2019)
42. G. W. Liang, L. H. Zeng, Y. H. Tsang, L. L. Tao, C. Y. Tang, P. K. Cheng, H. Long, X. Liu, J. Li, J. L. Qu, and Q. Wen, Technique and model for modifying the saturable absorption (SA) properties of 2D nanofilms by considering interband exciton recombination, *J. Mater. Chem. C* 6(28), 7501 (2018)
43. Q. S. Guo, A. Pospischil, M. Bhuiyan, H. Jiang, H. Tian, D. Farmer, B. C. Deng, C. Li, S. J. Han, H. Wang, Q. F. Xia, T. P. Ma, T. Mueller, and F. N. Xia, Black phosphorus mid-infrared photodetectors with high gain, *Nano Lett.* 16(7), 4648 (2016)
44. W. He, L. L. Kong, P. Yu, and G. W. Yang, Record-high work-function p-type $CuBiP_2Se_6$ atomic layers for high-photoresponse van der Waals vertical heterostructure phototransistor, *Adv. Mater.* 35(14), 2209995 (2023)
45. L. H. Zeng, D. Wu, S. H. Lin, C. Xie, H. Y. Yuan, W. Lu, S. P. Lau, Y. Chai, L. B. Luo, Z. J. Li, and Y. H. Tsang, Controlled synthesis of 2D palladium diselenide for sensitive photodetector applications, *Adv. Funct. Mater.* 29(1), 1806878 (2019)
46. D. Wu, J. W. Guo, J. Du, C. X. Xia, L. H. Zeng, Y. Z. Tian, Z. F. Shi, Y. T. Tian, X. J. Li, Y. H. Tsang, and J. S. Jie, Highly polarization-sensitive, broadband, self-powered photodetector based on graphene/$PdSe_2$/germanium heterojunction, *ACS Nano* 13(9), 9907 (2019)